CONTRAST MEDIA & MOLECULAR IMAGING

Received: 30 January 2015, Revised: 29 August 2015, Accepted: 11 October 2015, Published online in Wiley Online Library: 24 November 2015

(wileyonlinelibrary.com) DOI: 10.1002/cmmi.1673

Characterization of magnetic nanoparticles from *Magnetospirillum Gryphiswaldense* as potential theranostics tools

T. Orlando[a,b]*†, S. Mannucci[c], E. Fantechi[d], G. Conti[c], S. Tambalo[c], A. Busato[c], C. Innocenti[d], L. Ghin[e], R. Bassi[e], P. Arosio[f], F. Orsini[f], C. Sangregorio[g], M. Corti[a], M. F. Casula[h], P. Marzola[i], A. Lascialfari[f] and A. Sbarbati[c]

We investigated the theranostic properties of magnetosomes (MNs) extracted from magnetotactic bacteria, promising for nanomedicine applications. Besides a physico-chemical characterization, their potentiality as mediators for magnetic fluid hyperthermia and contrast agents for magnetic resonance imaging, both *in vitro* and *in vivo*, are here singled out. The MNs, constituted by magnetite nanocrystals arranged in chains, show a superparamagnetic behaviour and a clear evidence of Verwey transition, as signature of magnetite presence. The phospholipid membrane provides a good protection against oxidation and the MNs oxidation state is stable over months. Using an alternate magnetic field, the specific absorption rate was measured, resulting among the highest reported in literature. The MRI contrast efficiency was evaluated by means of the acquisition of complete NMRD profiles. The transverse relaxivity resulted as high as the one of a former commercial contrast agent. The MNs were inoculated into an animal model of tumour and their presence was detected by magnetic resonance images two weeks after the injection in the tumour mass. Copyright © 2015 John Wiley & Sons, Ltd.

Keywords: magnetosomes; relaxometry; contrast agent; MRI, hyperthermia; theranostics

1. INTRODUCTION

Theranostics is an innovative method combining diagnosis and therapy which is expected to have a relevant impact in the fight against cancer. By eliminating the clinical multi-step procedures, theranostics could reduce the delays among diagnosis and therapy. The use of nanoparticles properly labelled to recognize tumour cells might allow the simultaneous imaging and the effective local treatment of diseases (1). Among the different types of nanoparticles, iron oxide nanoparticles are considered to be promising candidates as effective tools for cancer theranostics due to their superparamagnetic behaviour combined to their relatively low toxicity (2-4).

Over the last decade, several magnetic particles having a maghemite or magnetite core have been proposed for biomedical applications. They can be used as contrast agents for magnetic resonance imaging (MRI) (5), mediators for magnetic fluid hyperthermia (MFH) (6), and carriers for drug delivery (7). Even if some of them have good performances in two or more of these tasks, none of them is, to our knowledge, at the clinical stage as theranostic agent.

In addition to synthetic iron oxide nanoparticles, the use of magnetosomes (MNs) in biomedicine has also been recently proposed (8,9). These nanostructures, constituted by pure magnetite particles arranged in chains and surrounded by a phospholipid membrane (10,11), are naturally synthesized by magnetotactic bacteria under specific environmental conditions.

* *Correspondence to: Tomas Orlando, Max Planck Institute for Biophysical Chemistry, Am Fassberg 11, D-37077, Göttingen - Germany. E-mail: tomas.orlando@mpibpc.mpg.de*

† *T. Orlando and S. Mannucci contributed equally to this work.*

a *T. Orlando, M. Corti*
Department of Physics and INSTM, Università degli Studi di Pavia, Pavia, I-27100, Italy

b *T. Orlando*
Research Group EPR Spectroscopy, Max Planck Institute for Biophysical Chemistry, Göttingen, D-37077, Germany

c *S. Mannucci, G. Conti, S. Tambalo, A. Busato, A. Sbarbati*
Department of Neurological and Movement Science and INSTM, University of Verona, Verona, I-37134, Italy

d *E. Fantechi, C. Innocenti*
Department of Chemistry, 'Ugo Schiff' University of Florence and INSTM, Sesto Fiorentino (FI), I-50019, Italy

e *L. Ghin, R. Bassi*
Department of Biotechnology and INSTM, University of Verona, Verona, I-37134, Italy

f *P. Arosio, F. Orsini, A. Lascialfari*
Department of Physics and INSTM, Università degli Studi di Milano, Milano, I-20133, Italy

g *C. Sangregorio*
CNR-ICCOM and INSTM, Sesto Fiorentino (FI), I-50019, Italy

h *M. F. Casula*
Department of Chemical and Geological Science and INSTM, University of Cagliari, Monserrato (CA), I-09042, Italy

i *P. Marzola*
Department of Computer Science and INSTM, University of Verona, Verona, I-37134, Italy

Furthermore, MNs exhibit a great hyperthermic efficiency both *in vitro* and *in vivo*. For these reasons, MNs were considered as thermotherapy agent.

In this work, we present the use of magnetosomes as theranostic tool for combined cancer detection by magnetic resonance imaging and treatment through magnetic fluid hyperthermia. The structural and magnetic properties, the hyperthermic efficiency and the relaxometry profiles of MNs extracted from *Magnetospirillum Gryphiswaldense* bacteria have been investigated. In particular, we show that the MNs act as effective hyperthermia mediators when exposed to alternating magnetic fields of an amplitude of 17 kA/m and frequency 183 kHz, and as MRI negative contrast agents at the clinical fields 0.2 T and 1.5 T both *in vitro* and *in vivo* (8,12-14). The MRI contrast efficiency has been established by collecting, for the first time to our knowledge, the complete NMR-dispersion profiles of longitudinal and transverse relaxivities.

2. MATERIALS AND METHODS

2.1. *Magnetospirillum Gryphiswaldense* culture and MNs purification

Magnetospirillum Gryphiswaldense strain MSR-1, purchased from Deutsche Sammlung von Mikroorganismen und Zellkulturen GmbH (Leibniz-Institut DSMZ, Braunschweig, Germany), was cultured as described in Ref. 11. MNs were extracted and purified according to methods published by Grünberg (15,16). Briefly, *M. Gryphiswaldense* (10 g) bacteria were suspended in 50 mL of 50 mM HEPES–4 mM EDTA (pH 7.4) and disrupted using French-press. Non lysated materials were removed by centrifugation at 680 g for 5 min. The obtained lysate was passed through a magnetic separation column (MACS, MiltenyiBiotec) and finally MNs were eluted with 10 mM HEPES (pH 7.4) buffer. MNs were centrifuged at 28 0000 g for 12 h at 4 °C and the obtained pellet was incubated with 10 mM HEPES for 16 h at 4 °C to allow for solubilization. After purification, MNs were lyophilized and irradiated with γ-rays.

2.2. Chemical, structural, and morphological characterization

The crystal structure of the MNs extracted from *Magnetospirillum Gryphiswaldense* was studied by recording the X-ray diffraction (XRD) pattern within the range of 10 °–90 ° (2ϑ) using Cu Kα radiation on a Panalytical Empyrean diffractometer equipped with a focusing mirror on the incident beam and an X'Celerator linear detector. The scans were acquired in Bragg–Brentano geometry with a graphite monochromator on the diffracted beam. The magnetosomes were deposited on a silicon low background sample holder and air dried prior to measurement collection. The average crystallite size was calculated by applying the Scherrer formula (17), from the peak full width at half maximum (FWHM) corrected for instrumental broadening as determined on a standard LaB_6 sample. Phase identification was performed according to the Powder Diffraction Files (PDF) crystallographic database (18).

Transmission electron microscopy (TEM) images were recorded on a Hitachi H-7000 Microscope (Hitachi Group, Tokyo, Japan), operating at 125 kV, equipped with a tungsten thermionic electron source and with a AMT DVC (Thorlabs, Newton, New Jersey, USA) (2048x2048 pixel) Charge-Coupled Device (CCD) Camera. Prior to observation, the samples were dropped on a carbon-coated copper grid and air-dried. Chemical composition was determined by inductively coupled plasma atomic emission spectrometry (ICP-AES) using a Varian Liberty 200 spectrophotometer (Agilent Technologies, Santa Clara, CA, USA). Typical solutions for the analysis of Fe content were prepared by dissolving about 0.5 mg of magnetosome powder in 10 mL of a 1:1 mixture of concentrated HNO_3/HCl and diluting up to 50 mL. Thermal gravimetry (TG) and differential thermal analysis (DTA) were carried out using a Mettler-Toledo TG/SDTA 851 (Mettler-Toledo, Greifensee, Switzerland) in the range 25–1000 °C under oxygen flow (heating rate = 10 °C/min, flow rate = 50 mL/min).

2.3. Magnetic characterization

The magnetic properties of extracted MNs were investigated using a Quantum Design MPMS SQUID magnetometer (Quantum Design, San Diego, CA, USA) operating in the temperature range 2 K ÷ 300 K with an applied field up to 5 Tesla. Measurements were performed on freeze-dried powder samples hosted in a polytetrafluoroethylene (PTFE) sample holder. The recorded magnetic moments were normalized for the effective amount of iron obtained by ICP analysis and the magnetization values are reported in terms of $A{\cdot}m^2/kg$ of iron. Zero Field Cooled-Field Cooled (ZFC/FC) curves were obtained by measuring the temperature dependence of the magnetization after cooling the sample in presence (FC) or in absence (ZFC) of applied magnetic field.

2.4. Hyperthermic characterization

The hyperthermic properties of the extracted MNs were investigated through calorimetric measurements. The experimental set-up, composed by a 6 kW Fives Celes® power supply (Fives, Lautenbach, France), a water-cooled induction coil and a series of variable capacitors (420 nF - 4.8 nF), is able to produce an alternate magnetic field with variable frequency ν in the range of 50–400 kHz and with field amplitude up to 19.1 kA/m. The field parameters used in this work (183 kHz, 17.0 kA/m) were chosen in order to operate within the physiological limit, i.e. $H{\cdot}\nu < 5{\cdot}10^9\ A{\cdot}m^{-1}s^{-1}$, beyond which living tissues damages have been observed (12). A screw cap vial containing a magnetosomes dispersion in agarose gel at 0.25% w/w, so that the iron concentration was 0.017% w/w, was placed in the middle of the induction coil. The polystyrene sample holder was placed in a glass container thermostatized by circulating ethylene glycol, in order to keep the system at 37 °C. The temperature kinetics curve, i.e. temperature as a function of time, of the sample was recorded by an optical fiber thermometer connected to a digital temperature recorder (Fotemp®) (Optocon AG, Dresden, Germany) during the whole exposition to alternate magnetic field. The specific absorption rate (*SAR*) value was evaluated using the formula $SAR = (\sum_i m_i C_{pi}/m_{Me}) \cdot (\Delta T/\Delta t)$, where ΔT is the temperature increase in the time interval Δt, m_{Me} is the total mass of metal, m_i is the mass of the i-species and C_{pi} is the corresponding specific heat. The sum is extended to all the species in the sample, i.e. water, agarose and inorganic components. The two last contributions are found negligible with respect to that of water. Due to the low concentration of agarose, the specific heat of the gel was assumed to be equal to the one of water. The measurements were performed in non adiabatic conditions and the $\Delta T/\Delta t$ values were evaluated from the initial slope ($t \to 0$) of the temperature kinetic curves, considering a Δt much shorter than the time constant of the thermalization circuit.

2.5. Relaxivity measurements

Longitudinal and transverse nuclear relaxation times, T_1 and T_2 respectively, were measured in both aqueous solution and agarose gel dispersion (0.25% w/w) over a wide range of frequency (10 kHz - 60 MHz). The NMR signal detection and generation was obtained with a Stelar Smartracer fast-field-cycling relaxometer (Stelar, Mede, Italy) in the range 10 kHz - 10 MHz and with a Stelar Spinmaster spectrometer in the range 10 MHz - 60 MHz. Saturation Recovery and Carr Purcell Meiboom Gill (CPMG) pulse sequences were used for T_1 and T_2 measurements, respectively. In order to have a quantitative estimation of the efficiency as MRI contrast agent, the nuclear relaxivities were calculated as follows: $r_i = \left(\frac{1}{T_{i,meas}} - \frac{1}{T_{i,matrix}}\right)/C_{[Fe]}$ where $i = 1$, 2, and $C_{[Fe]}$ is the millimolar concentration of iron ions.

2.6. Contrast agent efficiency

Longitudinal and transversal relaxivities were measured in agarose gel phantoms (0.25%) containing different amounts of MNs using a Bruker Tomograph (Bruker, Karlsruhe, Germany) equipped with a 4.7 T, 33 cm bore horizontal magnet (Oxford Ltd., Oxford, UK). T_2 values were measured by a Multi Slice Multi Echo (MSME) sequence with TR = 3000 ms, TE = 4.5 ms, N echoes = 16, FOV = 3.5x3.5 cm^2, MTX = 128/128, Slice Thickness = 2.00 mm, N slice = 3.

For *in vivo* tests, nude homozygote male mice (Harlan Laboratories, Udine, Italy) were kept under standard environmental conditions (temperature, humidity, 12 h/12 h light/dark cycle, with water and food *ad libitum*) under veterinarian assistance. Animals handling and surgery were performed following a protocol approved by the Animal Care and Use Committee of the University of Verona (CIRSAL), and by the Italian Ministry of Health, in strict adherence to the European Communities Council (86/609/EEC) directives, minimizing the number of animals used and avoiding their suffering. For tumour implantation, human glioblastoma-astrocytoma i.e. epithelial-like cell line (U87MG) purchased by ATCC (Manassas, VA, USA), were cultured in Eagle's Minimum Essential Medium (EMEM) with 10% of Fetal Bovine Serum (FBS), 1% of a mix of penicillin/streptomycin 1:1 and 1% of L-glutamine 200 mM, in 25 cm^2 plates and incubated at 37 °C in humidified air with 5% CO_2. Media and L-glutamine were purchased by Sigma-Aldrich (Saint Louis, Missouri, USA), while serum and antibiotic mix were acquired by GIBCO (Thermo Fisher Scientific, Waltham, Massachusetts, USA). When at confluence, cells were treated with trypsin-EDTA 1% GIBCO (Thermo Fisher Scientific, Waltham, Massachusetts, USA), harvested and centrifuged at 1200 rpm for 5 min. The supernatant was discarded and the cellular pellet was resuspended in 1 mL of complete medium, placed in 75 cm^2 plates and incubated at 37 °C and 5% of CO_2 until 80% confluence was detectable.

One million U87MG cells, resuspended in 200 μL of sterile phosphate buffered saline (PBS), were subcutaneously injected in the right flank of anesthetized mice. 30 days after inoculation of tumour cells, mice were monitored by MRI to measure the tumour size; when tumour volume reached about 100 μL, 1 mg of MNs diluted in 100 μL of PBS were injected directly into the tumour mass using an intradermal needle (21G).

For *in vivo* imaging, animals were anesthetized by 1% isofluorane inhalation in a mixture of oxygen and nitrogen. Animals were placed in prone position over a heated bed and inserted into a 3.5 cm i.d. birdcage r.f. coil. T_2 and T_2* weighted images were acquired to detect the tumour and the presence of MNs. T_2 weighted images were acquired using a RARE 3D sequence with TR = 1200 ms, TE_{eff} = 47.5 ms, FOV = 5x2.5x2.5 cm^3, NEX = 1, MTX = 256/128/32, Slice Thickness = 0.78 mm. T_2* weighted images were acquired using a FLASH sequence with TR = 400 ms, TE = 4.4 ms, flip angle = 10°, FOV = 5x2.5 cm, NEX = 2, MTX = 256/128, NSLICES = 8, Slice Thickness = 2 mm.

3. RESULTS AND DISCUSSION

The structure and morphology of the MNs extracted from *Magnetospirillum Gryphiswaldense* was investigated by XRD and TEM. The X-ray diffraction pattern, reported in Figure 1a, can

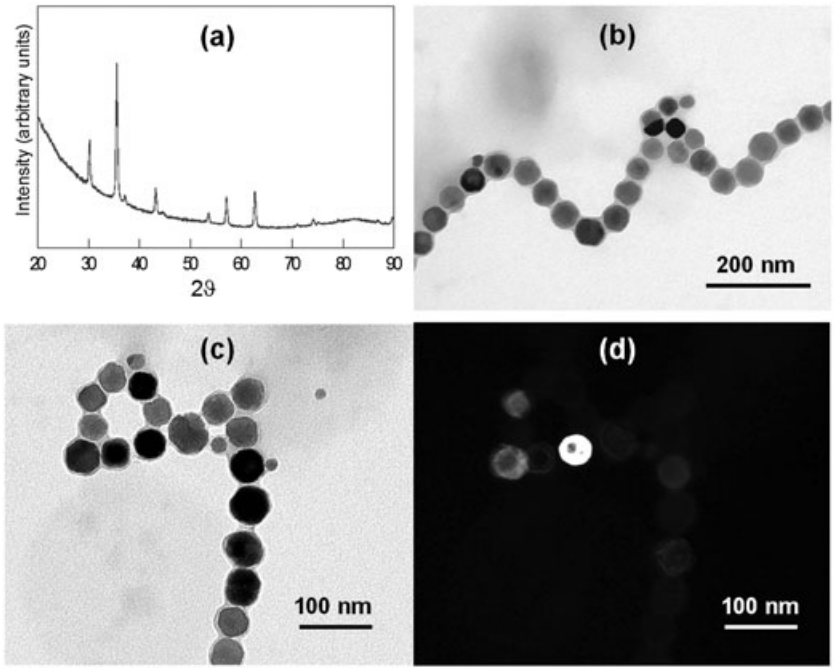

Figure 1. X-ray diffraction pattern (a) and representative Transmission electron microscopy image (b) MNs extracted from *Magnetospirillum Gryphiswaldense*. A closer inspection of a magnetic nanoparticle chain as obtained by TEM under bright field (c) and dark field (d) imaging is also reported.

be ascribed to a single crystalline phase with a spinel stucture which is consistent with the occurrence of magnetite Fe_3O_4 phase (PDF card 19-629). However, it should be pointed out that the occurrence of the fully oxidized iron oxide spinel phase, i.e. maghemite, cannot be ruled out based only on diffraction data (19). Peak broadening suggests the occurrence of a nanocrystalline phase, and in particular the average crystallite domain size as calculated from pattern profile analysis is 33 nm.

TEM investigation indicates the presence of cubic- and cubo-octahedral- shaped nanoparticles with a chain-like arrangement (Figure 1b). Comparison of the same area under bright (Figure 1c) and dark field mode (Figure 1d), where iso-oriented crystalline domains appear as bright contrast on a dark background, confirms that the nanoparticles are nanocrystalline and, in particular, that the particles are single crystals. A statistical analysis of the size over around 200 nanoparticles indicates that the largest size of the nanocrystals is peaked at 40 nm and ranges from 16 to 54 nm, as shown in Figure 2.

The field dependence of the magnetization is reported in Figure 3 both at 2.5 K and at 300 K. At low temperature, an open hysteresis loop is observed (see inset of Figure 3). The coercive field, $\mu_0 H_C$, is 42.8 mT, consistent with the literature values reported for magnetosomes (20) and synthetic iron oxide nanocubes of similar size (6). A small coercivity (2 mT) is also observed at room temperature. Similar values were reported in (13). The reduced remanent magnetization is $M_R = \frac{M_{0T}}{M_{5T}} = 0.45$, close to the one expected for a set of uniaxial nanoparticles whose axis is isotropically orientated (i.e. $M_R = 0.5$). An open hysteresis loop with reduced coercivity ($\mu_0 H_C$ =2.1 mT) is observed also at 300 K (Figure 3). Both curves are well saturated at high fields, being the saturation magnetizations $M_S = 139$ and 126 $A{\cdot}m^2/kg_{Fe}$ (corresponding to $M_S = 99$ and 89 $A{\cdot}m^2$ per kilogram of magnetite) at 2.5 and 300 K, respectively. Such values are very close to those of bulk magnetite (95 and 128 $A{\cdot}m^2/kg$ (21,22), for low and room temperatures, respectively), confirming the high crystallinity of the sample.

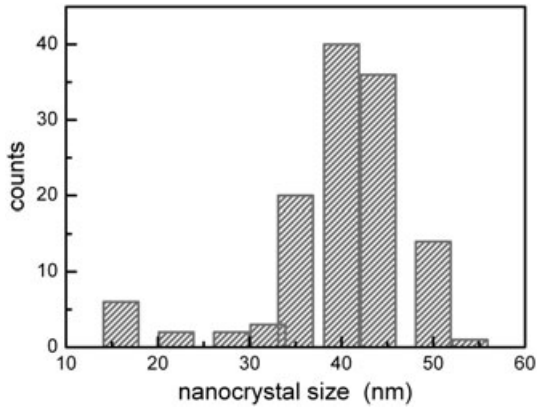

Figure 2. Size distribution obtained from TEM images. Due to the cubic and cubo-octahedral shape of the crystals, the maximum visible size was considered for each particle.

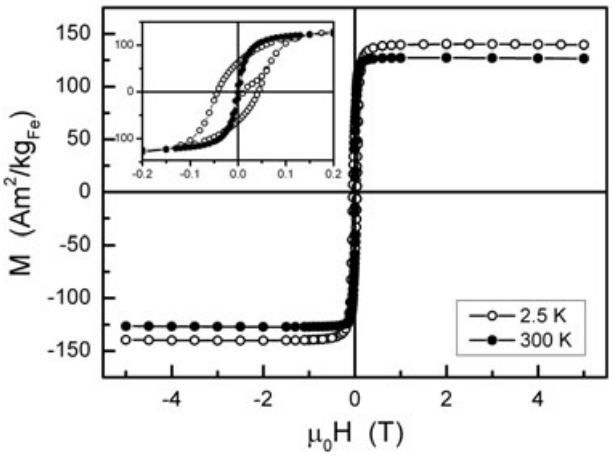

Figure 3. M vs. H curves of magnetosomes measured at 2.5 K (open circles) and 300 K (full circles). The magnification of both curves at low fields is reported in the inset.

Figure 4 shows the ZFC/FC magnetization curves for the MNs extracted from *Magnetospirillum Gryphiswaldense*. A discontinuity in the curves acquired at different fields can be clearly observed around 105 K: this could be an evidence for the Verwey transition (23,24), a crystallographic phase transition in metal oxides, which is expected to occur around 120 K for bulk magnetite in stoichiometric composition (Fe_2O_3) (25,26). This attribution is confirmed by the fact that its position is independent from the applied external magnetic field (Figure 4a). It should be noted that in bulk magnetite the transition occurs at ca. 120 K. However, a shift to lower temperature is often observed for nanometric particles, and is attributed to structural disorder and cation deficiency (24,26–28). On the other hand, the Verwey transition is generally not observed for small iron oxide NPs with mean size lower than 10-20 nm (29), due to their oxidation, facilitated by the large surface to volume ratio. For this reason, most of the time small NPs are composed by a mixture of iron oxides (magnetite/maghemite). A so clear evidence of the Verwey transition confirms that our sample is composed by magnetite NPs with average crystalline size of the order of that observed in the TEM analysis size (42 ± 9 nm) (15). Furthermore, the stability of the oxide phase was proved: indeed, as reported in Figure 4b, the Verwey transition is still clearly visible even after three months of storage of freeze-dried MNs at 4 °C in normal atmosphere. Most likely this is due to the phospholipid membrane that covers completely the magnetite crystals and prevents the contact with the air.

The blocking temperature T_B of the system, identifiable with the contact point between the ZFC curve and the FC one measured at low field, is above 300 K, as shown in the inset of Figure 4b. Considering the TEM average particle, T_B is expected to be much larger than the investigated temperature range (30).

The hyperthermic efficiency of extracted MNs was evaluated by recording the temperature kinetic curves of MNs dispersed in agarose gel and exposed to an alternate magnetic field of 17 kA/m and 183 kHz in amplitude and frequency, respectively. The kinetic curve, reported in Figure 5, shows that, despite the very low concentration of iron oxide (0.017% w/w), the temperature of the sample rises of about 5 °C in 5 minutes of exposition to the alternate magnetic field. This corresponds to a specific absorption rate (SAR) of 482.7 ± 50.8 W/g per mass of iron, a value that is among the highest reported in the literature (12,13,31,32).

The NMR longitudinal and transverse relaxivity results as a function of frequency are displayed in Figure 6, in comparison to those of Endorem, a former commercial 'negative' contrast agent. Both water and agarose gel dispersions were investigated. After some minutes, some reversible sedimentation phenomena were observed for MNs in water dispersion, but this issue did not compromise the NMR measurements, due to the fast measuring

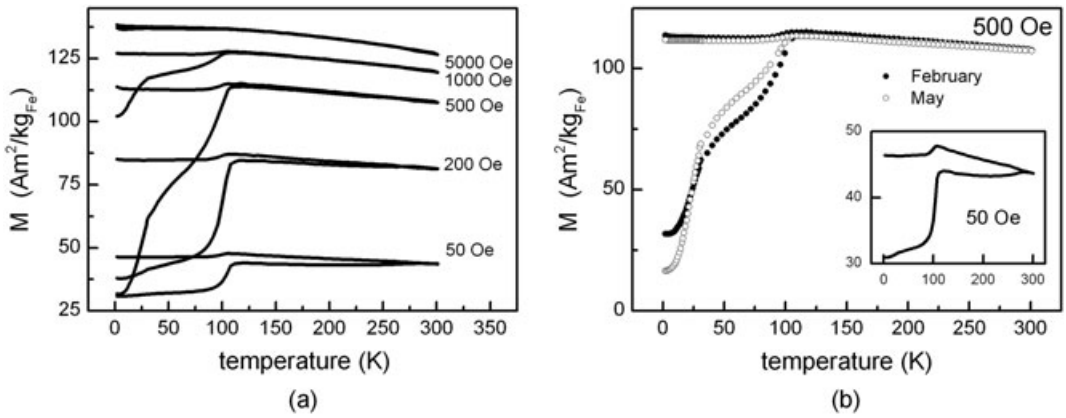

Figure 4. a) ZFC/FC curves collected at different magnetic fields for freeze-dried. b) ZFC/FC at 500 Oe collected for the same sample before and after a three months storage period at 4 °C. The signature of the Vervey transition is still evident, proving the good quality of the phospholipid membrane as shelter. Inset: ZFC/FC curves at 50 Oe: from here the blocking temperature is estimated to be above 300 K.

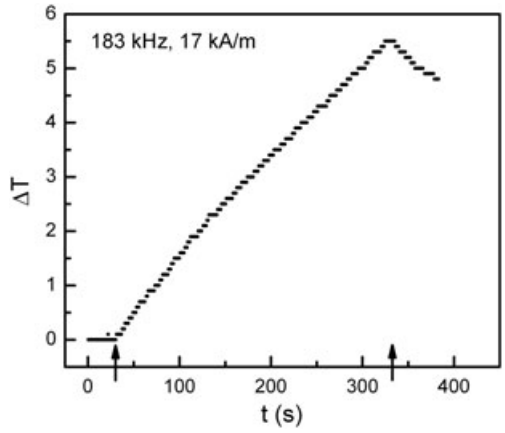

Figure 5. Temperature kinetics of the dispersion of MNs in agarose gel, exposed to an alternate magnetic field (183 kHz, 17 kA/m). The measurements were performed starting from body temperature (37 °C). The black arrows indicate the switch on and off of the magnetic field.

times (tens of seconds). The gel dispersion allows keeping the MNs fixed in the matrix, but also limits the mobility of the surrounding protons. Although MNs are composed by superparamagnetic crystals, the behaviour of the longitudinal relaxivity r_1 as a function of frequency is different from the NMR profile typical of iron oxide nanoparticles, in which a low frequency plateau, a maximum around 10 MHz and a monotonic decrease of r_1 at high frequency can be seen. On the contrary, MNs exhibit a monotonic decrease of r_1 as a function of frequency. This behaviour is independent from the dispersion matrix (water or agarose gel) and it is probably related to the MNs morphology and chain arrangement. For agarose dispersed MNs, the transverse relaxivity appears almost flat in the range of frequency 10-60 MHz. The quite low value is possibly due to the limited mobility of both the protons in the MNs surrounding and of the MNs themselves, which decreases the dephasing effect of the local magnetic field. On the other hand, the r_2 behaviour of MNs dispersed in water shows some frequency dependence. Remarkably, the r_2 values for MNs dispersed in water are higher than the ones of Endorem. As a consequence, MNs could be effectively used as negative contrast agent in magnetic resonance imaging.

The potential of MNs as MRI contrast agent was investigated *in vitro* and *in vivo* at 4.7 T with the Bruker tomograph, corresponding to the frequency $\nu = 200$ MHz for the proton. Magnetic resonance images of agarose gel phantoms containing different

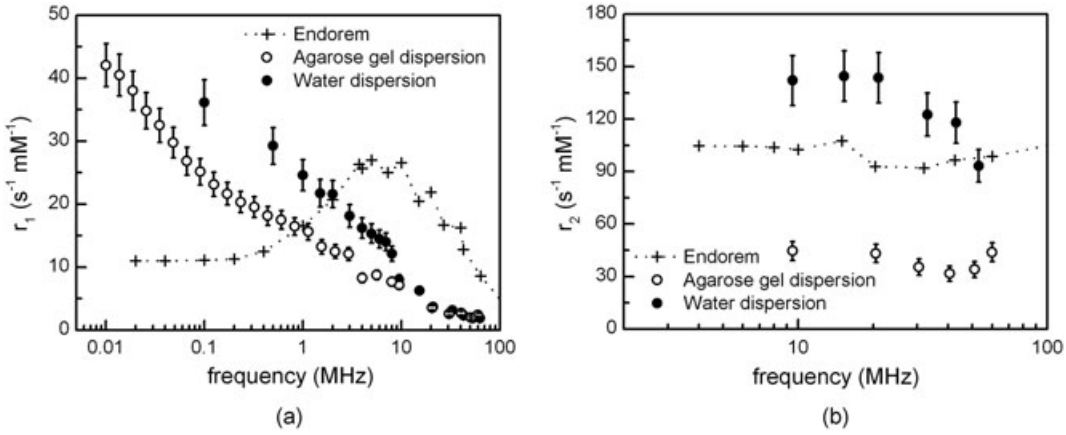

Figure 6. NMR dispersion profiles: (a) longitudinal relaxivity *r1* and (b) transverse relaxivity *r2* as a function of proton Larmor frequency for MNs dispersed in agarose gel (open circles) and in water (solid circles). The contribution of the matrix to the relaxation was considered in both cases. The relaxometry values of a former commercial contrast agent, i.e. Endorem, are shown for comparison purpose. The experimental error takes into account all the experimental procedures and was quantified as 8% of the absolute value.

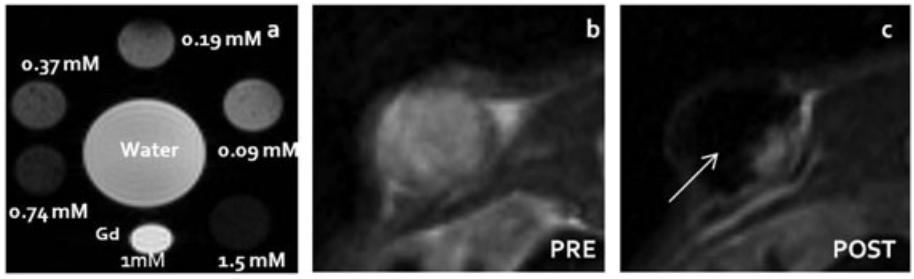

Figure 7. *In vitro* and *in vivo* contrast efficiency of MNs as MRI agents. (a) T2-weighted image of phantoms at different MNs concentrations (the values are reported in mM of iron). The iron content in our MNs samples determined by atomic absorption spectroscopy was 0.167 w/w. T2-weighted images of tumor tissue before (b) and 24 h after (c) MNs injection.

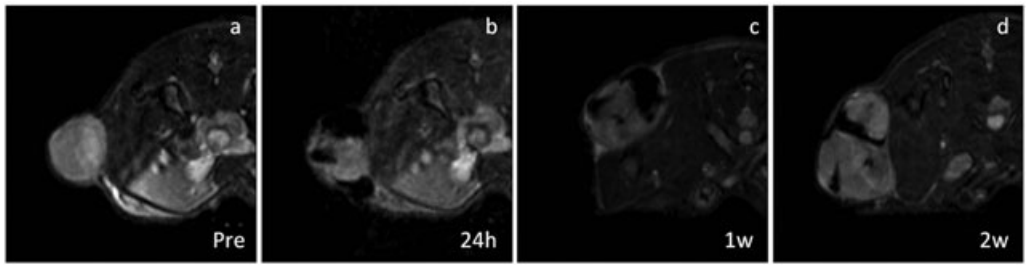

Figure 8. Time evolution of MNs signal *in vivo*. T2-weighted images of tumor (a) before the MNs injection, (b) 1 hour after, (c) 1 week after and (d) 2 weeks after the injection.

amounts of MNs are reported in Figure 7a. As expected, the signal intensity clearly depends on the MNs concentration. Quantitative measurements of T_1 and T_2 values for different MNs concentrations at 4.7 T allowed the determination of the transverse relaxivity $r_2 = 204 \pm 2\ s^{-1}\ mM^{-1}$. The great difference between r_2 at 60 MHz and the one at 200 MHz is due to the echo time commonly available in MRI scanners, which is too long to avoid the contribution of the proton diffusion. However, this measurement being a common practice, some observation can be done. In particular, for this field value the transverse relaxivity of MNs in agarose gel is higher than the one of Endorem ($r_2 = 94.8\ s^{-1}\ mM^{-1}$) (33) and comparable to other similar iron based contrast agents (e.g. Resovist, $r_2 = 151.0\ s^{-1}\ mM^{-1}$) (34). The observed high transverse relaxivity, as well as the high r_2/r_1 ratio, strongly confirms that the MNs could be efficient superparamagnetic contrast agents for MRI, also at higher fields.

This was experimentally confirmed by the *in vivo* T_2-weighted images. Images of U87MG xenografted mice acquired before and after injection of 1 mg of MNs diluted in 200 μL of PBS into the tumour mass are shown in Figure 7b and c. Thanks to the high transverse relaxivity, the presence of MNs is well detectable as a dark region. Furthermore, we investigated the evolution of the signal as a function of the time (see Figure 8): as one can see, the MNs remain detectable even after two weeks (Figure 8d).

4. CONCLUSIONS

In this work several techniques have been used to characterize magnetosomes naturally produced by the magnetotactic bacteria *Magnetospirillum gryphiswaldence*. From structural analysis, we verified that their magnetic cores are composed by magnetite single crystals arranged in chains and coated with a phospholipid membrane. The oxide phase is stable over months thanks to the shielding effect of the membrane. This was confirmed by the magnetic measurements, which showed an evident Verwey transition around 105 K. Due to the particles size, the blocking temperature is above 300 K.

The great potentiality of MNs as mediators for magnetic fluid hyperthermia was verified: the specific absorption rate (SAR) obtained after the application of an alternate magnetic field is 482.7 W/g, among the highest reported in literature. The NMRD profiles, acquired for MNs dispersed both in agarose gel and water, demonstrated good contrast efficiency as negative MRI contrast agents compared to Endorem, a former clinical contrast agent. An animal model of tumour was used for *in vivo* MRI tests. The high contrast efficiency allows to easily identify the region where the magnetosomes were injected, even after two weeks.

These results, together with the ones previously achieved (15), state how magnetosomes can represent a good platform to develop a multifunctional nanostructured material suitable for theranostics. Indeed, the possibility to combine the therapeutic effect of the released heat along with a higher contrast in MRI images is extremely interesting: this would allow monitoring the distribution of the particles in the tumour tissue and, at the same time, to have an immediate check of the hyperthermic treatment efficacy, through tumour volume measurements.

Acknowledgements

The authors would like to thank the Associazione Italiana per la Ricerca sul Cancro (AIRC) for funding under grant agreement No.11993. The financial support of Italian MIUR through project FIRB Riname RBAP114AMK is also acknowledged. C.S. E.F and C.I. are grateful to Maurizio Passaponti for the realization of glassware equipment for hyperthermia instrumentation.

REFERENCES

1. Davis ME, Chen ZG, Shin DM. Nanoparticle therapeutics: an emerging treatment modality for cancer. Nat. Rev. Drug Discov. 2008; 7: 771–782. doi:10.1038/nrd2614.
2. Colombo M, Carregal-Romero S, Casula MF, Gutiérrez L, Morales MP, Böhm IB, Heverhagen JT, Prosperi D, Parak WJ. Biological applications of magnetic nanoparticles. Chem. Soc. Rev. 2012; 41: 4306–4334. doi:10.1039/c2cs15337h.
3. Pankhurst Q, Thanh N, Jones S, Dobson J. Progress in applications of magnetic nanoparticles in biomedicine. J. Phys. D. Appl. Phys. 2009; 42: 224001. doi:10.1088/0022-3727/42/22/224001.
4. Santhosh PB, Ulrih NP. Multifunctional superparamagnetic iron oxide nanoparticles: Promising tools in cancer theranostics. Cancer Lett. 2013; 336: 8–17. doi:10.1016/j.canlet.2013.04.032.
5. Arosio P, Thévenot J, Orlando T, Orsini F, Corti M, Mariani M, Bordonali L, Innocenti C, Sangregorio C, Oliveira H, Lecommandoux S, Lascialfari A, Sandre O. Hybrid iron oxide-copolymer micelles and vesicles as contrast agents for MRI: impact of the nanostructure on the relaxometric properties. J. Mater. Chem. B 2013; 1: 5317–5328. doi:10.1039/c3tb00429e.
6. Lartigue L, Innocenti C, Kalaivani T, Awwad A, Sanchez Duque MDM, Guari Y, Larionova J, Guérin C, Montero JLG, Barragan-Montero V, Arosio P, Lascialfari A, Gatteschi D, Sangregorio C. Water-dispersible sugar-coated iron oxide nanoparticles. An evaluation of their relaxometric and magnetic hyperthermia properties. J. Am. Chem. Soc. 2011; 133: 10459–10472. doi:10.1021/ja111448t.
7. Sanson C, Diou O, Thévenot J, Ibarboure E, Soum A, Brulet A, Miraux S, Thiaudière E, Tan S, Brisson A, Dupuis V, Sandre P, Lecommandoux S. Doxorubicin loaded magnetic polymersomes: theranostic nanocarriers for MR imaging and magneto chemotherapy. ACS Nano 2011; 5: 1122–1140. doi:10.1021/nn102762f.
8. Alphandéry E, Faure S, Seksek O, Guyot F, Chebbi I. Chains of magnetosomes extracted from AMB-1 magnetotactic bacteria for application in alternative magnetic field cancer therapy. ACS Nano 2011; 5: 6279–6296. doi:10.1021/nn201290k.
9. Benoit MR, Mayer D, Barak Y, Chen IY, Hu W, Cheng Z, Wang SX, Spielman DM, Gambhir SS, Matin A. Visualizing implanted tumors in mice with magnetic resonance imaging using magnetotactic bacteria. Clin. Cancer Res. 2009; 15: 5170–5177. doi:10.1158/1078-0432.CCR-08-3206.
10. Blakemore R. Magnetotactic bacteria. Science 1975; 190: 377–379. doi:10.1126/science.170679.
11. Yan L, Zhang S, Chen P, Liu H, Yin H, Li H. Magnetotactic bacteria, magnetosomes and their application. Microbiol. Res. 2012; 167: 507–519. doi:10.1016/j.micres.2012.04.002.
12. Hergt R, Dutz S. Magnetic particle hyperthermia. Biophysical limitations of a visionary tumor therapy. J. Magn. Magn. Mater. 2007; 311: 187–192. doi:10.1016/j.jmmm.2006.10.1156.
13. Hergt R, Hiergeist R, Zeisberger M, Schüler D, Heyen U, Hilger I, Kaiser WA. Magnetic properties of bacterial magnetosomes as potential diagnostic and therapeutic tools. J. Magn. Magn. Mater. 2005; 293: 80–86. doi:10.1016/j.jmmm.2005.01.047.
14. Alphandéry E, Chebbi I, Guyot F, Durand-Dubief M. Use of bacterial magnetosomes in the magnetic hyperthermia treatment of tumours: A review. Int. J. Hyperthermia 2013; 29: 801–809. doi:10.3109/02656736.2013.821527.
15. Mannucci S, Ghin L, Conti G, Tambalo S, Lascialfari A, Orlando T, Benati D, Bernardi P, Betterle N, Bassi R, Marzola P, Sbarbati A. Magnetic Nanoparticles from Magnetospirillum gryphiswaldense Increase the Efficacy of Thermotherapy in a Model of Colon Carcinoma. PLoS One 2014; 9: e108959. doi:10.1371/journal.pone.0108959.
16. Grünberg K, Müller EC, Otto A, Reszka R, Linder D, Kube M, Reinhardt R, Schüler D. Biomedical and proteomic analysis of the magnetosome membrane in Magnetospirillum gryphiswaldense. Appl. Environ. Microbiol. 2004; 70: 1040–1050. doi:10.1128/AEM.70.2.1040-1050.2004.
17. Klug HP, Alexander LE. X-ray Diffraction Procedures. Wiley: New York, 1974.
18. ICDD International Centre for Diffraction Data. Park Lane. Swarthmore: USA, 1601.
19. Corrias A, Mountjoy G, Loche D, Puntes V, Falqui A, Zanella M, Parak WJ, Casula MF. Identifying spinel phases in nearly monodisperse iron oxide colloidal nanocrystal. J. Phys. Chem. C 2009; 113: 18667–18675. doi:10.1021/jp9047677.
20. Alphandery E, Ngo AT, Lefevre C, Lisiecki I, Wu LF, Pileni MP. Difference between the magnetic properties of the magnetotactic bacteria and those of the extracted magnetosomes: influence of the distance between the chains of magnetosomes. J. Phys. Chem. C 2008; 112: 12304–12309. doi:10.1021/jp800408t.
21. Schieber MM. Iron oxides and their compounds. In Experimental Magnetochemistry, Wohlfarth, EP (ed). North-Holland Publishing Company: Amsterdam, 1967.
22. Dunlop DJ, Özedmir Ö. Rock Magnetism: Fundamental and Frontiers. Cambridge University Press: Cambridge, 2001.
23. Verwey EJW, Haayman PW. Electronic conductivity and transition point of magnetite ("Fe_3O_4"). Physica 1941; 8(9): 979–987. doi:10.1016/S0031-8914(41)80005-6.
24. Prozorov R, Prozorov T, Mallapragada SK, Narasimhan B, Williams TJ, Bazylinski D a. Magnetic irreversibility and the Verwey transition in nanocrystalline bacterial magnetite. Phys. Rev. B. Phys. 2007; 76: 054406. doi:10.1103/PhysRevB.76.054406.
25. Aragón R, Buttrey DJ, Shepherd JP, Honig JM. Influence of nonstoichiometry on the Verwey transition. Phys. Rev. B 1985; 31: 430–436. doi:10.1103/PhysRevB.31.430.
26. García J, Subías G. The Verwey transition - a new perspective. J. Phys. Condens. Matter 2004; 16: R145–R178. doi:10.1088/0953-8984/16/7/R01.
27. Weiss BP, Kim SS, Kirschvink JL, Kopp RE, Sankaran M, Kobayashi A, Komelli A. Ferromagnetic resonance and low-temperature magnetic tests for biogenic magnetite. Earth Planet. Sci. Lett. 2004; 224: 73–89. doi:10.1016/j.epsl.2004.04.024.
28. Pan Y, Petersen N, Winkhofer M, Davila A, Liu Q, Frederichs T, Hanzlik M, Zhu R. Rock magnetic properties of uncultured magnetotactic bacteria. Earth Planet. Sci. Lett. 2005; 237: 311–325. doi:10.1016/j.epsl.2005.06.029.
29. Santoyo Salazar J, Perez L, de Abril O, Truong Phuoc L, Ihiawakrim D, Vazquez M, Greneche J-M, Begin-Colin S, Pourroy G. Magnetic Iron Oxide Nanoparticles in 10–40 nm Range: Composition in Terms of Magnetite/Maghemite Ratio and Effect on the Magnetic Properties. Chem. Mater. 2011; 23: 1379–1386. http://doi.org/10.1021/cm103188a.
30. Batlle X, Labarta A. Finite-size effects in fine particles: magnetic and transport properties. J. Phys. D. Appl. Phys. 2002; 35: R15–R42. doi:10.1088/0022-3727/35/6/201.
31. Alphandéry E, Faure S, Raison L, Duguet E, Howse PA, Bazylinski DA. Heat production by bacterial magnetosomes exposed to an oscillating magnetic field. J. Phys. Chem. C 2011; 115: 18–22. doi:10.1021/jp104580t.
32. Serantes D, Simeonidis K, Angelakeris M, Chubykalo-Fresenko O, Marciello M, del Puerto Morales M, Baldomir D, Martinez-Boubeta C. Multiplying magnetic hyperthermia response by nanoparticle assembling". J. Phys. Chem. C 2014; 118: 5927–5934. doi:10.1021/jp410717m.
33. Masotti A, Pitta A, Ortaggi G, Corti M, Innocenti C, Lascialfari A, Marinone M, Marzola P, Daducci A, Sbarbati A, Micotti E, Orsini F, Poletti G, Sangregorio C. Synthesis and characterization of polyethylenimine-based iron oxide composites as novel contrast agents for MRI. Magn. Reson. Mater. Phys. 2009; 22: 77–87. doi:10.1007/s10334-008-0147-x.
34. Wang Y-XJ. Superparamagnetic iron oxide based MRI contrast agents: Current status of clinical application. Quant. Imaging Med. Surg. 2011; 1: 35–40. doi:10.3978/j.issn.2223-4292.2011.08.03.

